Traceable Waveform Calibration With a Covariance-Based Uncertainty Analysis

Paul D. Hale, *Senior Member, IEEE*, Andrew Dienstfrey, Jack C. M. Wang, Dylan F. Williams, *Fellow, IEEE*, Arkadiusz Lewandowski, *Student Member, IEEE*, Darryl A. Keenan, and Tracy S. Clement, *Senior Member, IEEE*

***Abstract*—We describe a method for calibrating the voltage that a step-like pulse generator produces at a load at every time point in the measured waveform. The calibration includes an equivalent-circuit model of the generator that can be used to determine how the generator behaves when it is connected to arbitrary loads. The generator is calibrated with an equivalent-time sampling oscilloscope and is traceable to fundamental physics via the electro-optic sampling system at the National Institute of Standards and Technology. The calibration includes a covariance-based uncertainty analysis that provides the uncertainty at each time in the waveform vector and the correlations between the uncertainties at the different times. From the calibrated waveform vector and its covariance matrix, we calculate pulse parameters and their uncertainties. We compare our method with a more traditional parameter-based uncertainty analysis.**

***Index Terms*—Covariance matrices, deconvolution, oscilloscopes, pulse measurements, signals, uncertainty, waveforms.**

I. Introduction

In THIS paper, we describe a new methodology for measuring a repetitive step-like signal with an equivalent-time sampling oscilloscope and for calibrating these measurements to obtain the voltage or current that the signal generator delivers to an arbitrary load. The calibration is traceable to fundamental physics through the electro-optic sampling system at the National Institute of Standards and Technology (NIST). The methodology includes a novel covariance-matrix uncertainty analysis that characterizes the uncertainty in the waveform at every time point in the measured waveform epoch as well as pairwise correlations at different times.

Calibrated signals such as combs [1], multisines [2], and step-like pulses [3]–[5] are often used to measure the transfer function of various electronic or optoelectronic components, oscilloscopes, and other waveform recording devices. In the step-like pulse measurements that we focus on in this paper, it is sometimes adequate to quantify the performance of the system under test simply in terms of pulse parameters, such as transition duration, amplitude, and settling duration (e.g., [3]–[5]). In other applications, more detailed characterization of the waveform and its features is necessary. This is true, for example, when comparing different measurement systems (e.g., [6] and [7]), measuring high-speed communications signals (e.g., [7]–[9]), and probing high-speed circuits (e.g., [10]). Details of these experiments may not be completely characterized by a few waveform parameters. Furthermore, as the measurement bandwidth increases into the microwave and millimeter-wave regions, impedance mismatch, loss, and dispersion must be accounted for because they can cause complicated distortions in the signal at these frequencies. In the past, many calibration services have treated these effects in an ad hoc manner.

In the following, we describe traceable calibration of the whole waveform. That is, our calibration procedure returns an estimate of the waveform value at every time point in the measured waveform epoch, as well as a characterization of its uncertainty and pairwise correlations. Once the waveform is calibrated, various metrics that characterize the waveform can be calculated. The pulse parameters in [3] are examples of scalar waveform metrics that are commonly used. Our approach is fundamentally different from previous work in waveform metrology (such as in [3]–[5] and [11]). In our approach, we divide the measurement of waveform metrics into two steps. We first calibrate the waveform (a vector) and estimate its covariance matrix based on a characterization of various sources of uncertainty in the measurement system. Calibration of the waveform includes use of the generator and sampler impedances (as in [12] and [13]), along with the waveform measurement, to derive an equivalent-circuit model of the generator. This model is used to determine the waveform the generator will deliver to an arbitrary load. Then, algorithms, such as those described in [14] and [15], can be used to "project" the waveform vector onto an arbitrary scalar or vector waveform metric. Standard multivariate propagation of uncertainty [16], employing the linearization of the algorithms and the waveform covariance matrix, is then used to find the uncertainty in the desired metric.

While traditional waveform uncertainty analyses (see, e.g., [11]) propagate uncertainty directly from the physical source of uncertainty in the measurement system to a specific pulse parameter, we propagate uncertainty from the source of uncertainty to the waveform uncertainty, and then propagate from the waveform uncertainty to the uncertainty of the waveform metric. Daboczi advocated a similar approach in [17] but did not propose a method for calculating pulse parameters or other waveform metrics from the calibrated waveform or for propagating their uncertainty. Analytically, the two-step uncertainty analysis that we propose may be viewed as uncertainty propagation using the chain rule for derivatives. Separating the steps of calculating waveform and calculating the uncertainties makes

Manuscript received September 22, 2008; revised March 5, 2009. First published May 26, 2009; current version published September 16, 2009. This work is a contribution of the National Institute of Standards and Technology (NIST) and is not subject to copyright in the United States. The Associate Editor coordinating the review process for this paper was Dr. Rik Pintelon.

The authors are with NIST, Boulder, CO 80305 USA.

Color versions of one or more of the figures in this paper are available online at http://ieeexplore.ieee.org.

Digital Object Identifier 10.1109/TIM.2009.2018012

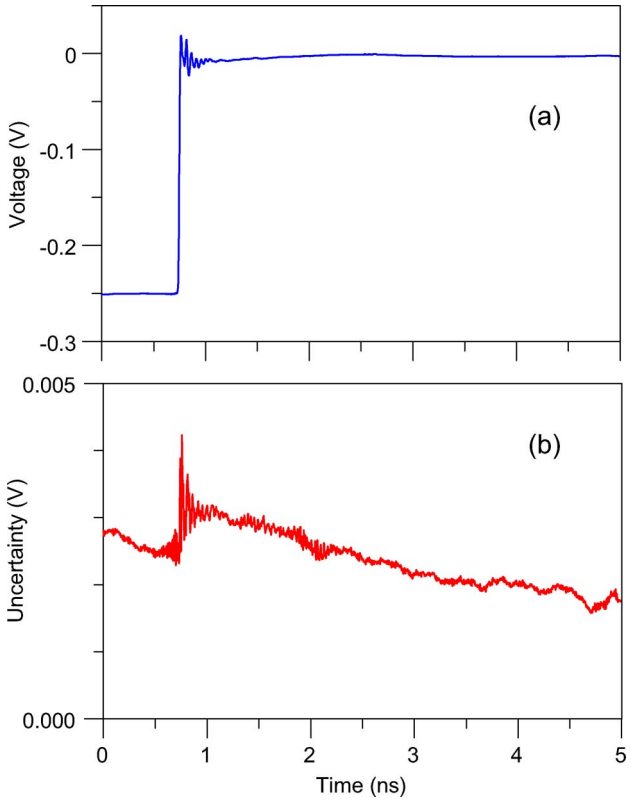

Fig. 1. (a) Calibrated waveform that the pulse generator delivers to a 50-Ω load at its 3.5-mm connector. (b) Standard uncertainty at every point in the waveform. The uncertainty is the square root of the diagonal elements of the covariance matrix.

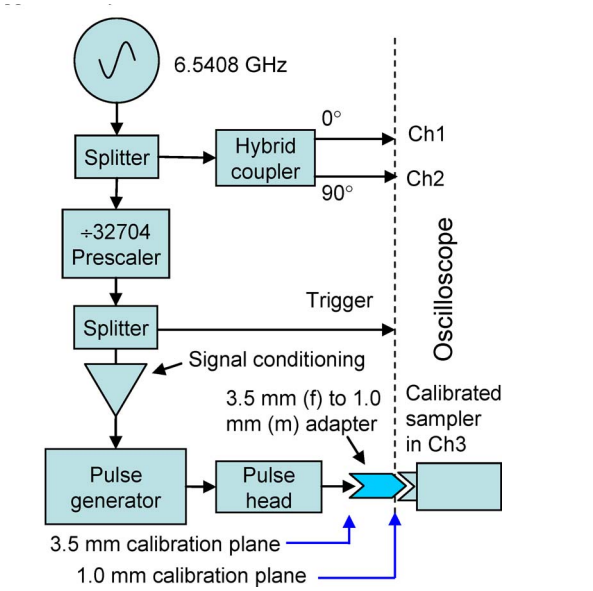

Fig. 2. Schematic diagram of the pulse measurement apparatus. The synthesized signal generator produces sine waves that are used to correct for jitter and timebase distortion in the equivalent-time oscilloscope. The signal conditioning block includes a delay line (about 32 ns), a limiting amplifier, and a bias-T. Three 3.5–1.0-mm adapters (G, R, B) and three samplers (1, 2, 3) are used to characterize our ability to correct for changes in the measurement system and possible effects of high-order modes.

our approach convenient for characterizing a broad class of waveforms beyond those discussed in [3] and [11], enabling the user of the calibrated waveform generator to calculate arbitrary waveform metrics, with rigorous uncertainty estimates if desired. Finally, our covariance-based techniques can be used outside the calibration laboratory environment to characterize various stochastic properties of signals.

Although our methodology can be applied to a broad range of waveforms, we demonstrate our measurement strategy in this paper by calibrating the step-like pulse generated by a commonly used pulse generator, allowing us to compare results with an analysis similar to that used in [11]. The 10%–90% and 20%–80% pulse transition durations of the voltage that the generator produces at a 50-Ω load are about 15 and 10 ps, respectively, while the pulse amplitude is about 248 mV. We describe the apparatus used for the measurements (previously outlined in [18]) and the signal processing that we use to correct for systematic errors. The result of our calibration is shown in Fig. 1.

The waveform approach also requires new methods for averaging the measured waveform vectors and for calculating the covariance matrices that describe their repeatability and reproducibility.[1] We present these methods and show that pulse parameters and their uncertainties, found using the averaged waveform and its covariance, agree with the more traditional approach of calculating the mean pulse parameter and its uncertainty obtained from each measured waveform (as in [3, Sec. 5.9]). We end this paper with a discussion of a 2×1 vector waveform metric example whose elements are the state levels of the two-level pulse of this work.

[1]We define repeatability as the short-term variations observed while attempting to keep the measurement conditions the same. We define reproducibility as the variation in measurements due to changes in the measurement apparatus while attempting to keep all other measurement conditions the same.

II. Waveform Measurement

A. Apparatus and Correction for Timebase Errors

Fig. 2 shows our measurement apparatus. Our apparatus and measurement procedures are designed to correct for systematic effects in the measurement system and to quantify various sources of uncertainty that are beyond our control. The measured waveform has errors in both the time and voltage of each sample, and we compensate errors in both dimensions in our analysis.

We use the NIST timebase correction technique [19] to correct for jitter and timebase distortion in the measurement system. The synthesized signal generator produces 6.5408-GHz sine waves that are used to correct for jitter and timebase distortion. The 90° hybrid coupler produces quadrature sinusoids that are measured on channels 1 and 2. The prescaler produces pulses with a fast transition at a repetition rate at which the pulse generator will trigger (200 kHz). This pulse is used to trigger the oscilloscope, and a replica of the pulse is delayed (as in [20]), passes through a limiting amplifier to steepen the transition after the lossy delay line, and is then used to trigger the pulse generator and remote pulse head (collectively referred to here as the "pulse generator" or the "generator"). The resulting pulse from the generator is measured on channel 3

simultaneously with the sinusoids on channels 1 and 2. The system then transfers the data to a computer for postprocessing.

Because all of the samplers in the oscilloscope are activated by the same trigger pulse and timebase, the timing errors in all the channels in the oscilloscope mainframe are nearly identical. The NIST timebase correction software [21] uses an orthogonal distance regression technique [22] to fit the sinusoids[2] and estimate the timing error in their measurement. We then use this estimate to compensate for the timing error in each sample of the signal of interest (from the pulse generator). This procedure eliminates the need to separately correct for timebase distortion and jitter.

The timebase of the oscilloscope we use has significant distortion, including discontinuities every 4 ns. Although the timebase correction procedure compensates for this discontinuity, we still take caution to minimize residual errors by positioning the pulse so that discontinuities in the timebase do not occur near the fast transition or in a region of the pulse where there is a significant structure. By adjusting the delay (about 32 ns) between the oscilloscope trigger and the pulse generator trigger, we can shift the time at which the fast transition of the pulse that we are testing occurs relative to the timebase discontinuity.

Voltage errors must also be compensated. Static voltage errors are reduced by using the built-in dc calibration of the oscilloscope before each set of measurements to correct for gain errors, offset errors, and "nonlinear distortion"—the manufacturer's term for nonuniformity in the discrete levels of the oscilloscope's analog-to-digital converter. The finite-impulse response (dynamic error) of the oscilloscope is calibrated by use of the techniques in [13] and [23], and then the measured step waveform is corrected for the oscilloscope response, as outlined below in Sections III and IV.

B. Signal Processing Considerations

The waveform epoch must be carefully considered to maintain accuracy while compensating for timebase error, impedance mismatch, and the dynamic response of the sampler. The measured waveform (not shown) has a structure, approximately 1–2 ns after the main transition, which is caused by the impedance mismatch of the oscilloscope and the pulse generator, and it is important to choose the waveform epoch such that all the significant reflections are captured. This is different from many experiments where reflections are intentionally windowed out of the measured data or where impedance mismatch is ignored. The epoch duration and the occurrence of the fast transition in the epoch must also be chosen such that settling effects are captured to an acceptable level of accuracy. Finally, the deconvolution process used to compensate for the oscilloscope and adapters shifts the waveform in time. Significant features of the waveform must occur in the waveform epoch such that they are not displaced by deconvolution to a time that is earlier than the beginning of the measured epoch. In our measurement, we place the transition at roughly 1 ns after the beginning of the measured waveform.

The measured waveform is initially sampled at 4096 points in a 5.1-ns epoch. After correction for timebase errors, the corrected epoch duration (for our oscilloscope) is compressed slightly and the time interval between samples is nonuniform. To facilitate further signal processing, we linearly interpolate the corrected waveform to $N = 2048$ evenly spaced points in a 5.0-ns epoch that is entirely inside the initially measured 5.1-ns epoch. This subsampling procedure avoids possible extrapolation at the endpoints of the waveform. The discrete Fourier transform (DFT) of the 5-ns waveform sampled at 2048 equispaced time points results in spectral information from dc to 204.8 GHz at frequencies spaced by 200 MHz. We choose this sampling rate and the associated Nyquist frequency (2.44 ps and 204.8 GHz) such that there is minimal aliasing in the measured waveforms that we discuss here (see Fig. 10). We experimented with higher order interpolation schemes and found that the present sampling rate relative to the waveform features was chosen such that there was no significant difference. This could change when measuring waveform generators with faster transitions (see [24] and [25]).

We acquire a data set consisting of $K = 100$ waveforms, as described in Section II-A, and average them to achieve an approximately 20-dB improvement in the signal-to-noise ratio. After averaging, the signal-to-noise ratio in the ramp-subtracted signal is about 80 dB at low frequencies and falls to 0 dB between 70 and 80 GHz (see discussion and Fig. 10). We also acquire statistics on the 100 waveforms to characterize the additive noise and the residual jitter and drift after timebase correction.

III. Oscilloscope and Adapter Calibration

We next correct for the dynamic response of our measurement system. We model the system as linear and time invariant. Therefore, the time-domain waveform vector $\mathbf{y}$, once corrected for timebase errors and averaged, is a discretized convolution of the pulse generator's output signal $x(t)$ and the system response function $a(t)$.[3] That is

$$\mathbf{y} = \mathbf{a}\mathbf{x} \tag{1}$$

where $\mathbf{a}$ is a matrix form of the (time domain) convolution operation. The system response function consists of the following two parts [13]: 1) the response function of the oscilloscope when connected to an ideal 50-Ω source and 2) the effects of the impedance of the source, adapter, and oscilloscope. We now consider the calibration of these two contributions and their combination, resulting in the operator $\mathbf{a}$. Section IV will be concerned with the deconvolution problem, i.e., solving (1) for a discretized representation $\mathbf{x}$ of the generator's output.

A. Oscilloscope Response Function

We use a photodiode with a calibrated electrical output pulse to determine the oscilloscope's impulse response [23].

[2]We also measure sinusoids at 6.5 and 6.6 GHz to estimate the timebase distortion as an initial guess for the orthogonal-distance regression algorithm.

[3]We denote vectors and matrices in bold font and continuous functions of time in italics.

The photodiode generates an electrical pulse at its 1.0-mm coaxial output when it is excited with a short optical pulse at its fiber input. We calibrated the electrical pulse generated by the photodiode at its 1.0-mm output using NIST's electro-optic sampling system with the procedures described in [15], [26], and [27]. This calibration is mismatch corrected to determine the voltage that the photodiode would supply to an ideal 50-Ω load. The photodiode calibration allows for oscilloscope calibration up to a scale factor. The absolute magnitude response of the oscilloscope is scaled using a swept-sine technique similar to those described in [12] and [28].

The calibration is reported at frequencies between dc and 110 GHz. The high-frequency limitation arises from limits on our present impedance characterization. However, this strict bandwidth cutoff exceeds the useable spectral content of our pulse generator and is not a concern in our present analysis.

In order to maximize the bandwidth of the oscilloscope calibration, we dedicate a 1.0–1.85 or 2.4 mm adapter to each of our oscilloscope samplers, as shown in Fig. 2. This provides a single-mode interface up to 110 GHz, allowing us to determine the response of the oscilloscope and the adapter to a 50-Ω source at the 1.0-mm coaxial reference plane to 110 GHz. We also calculate the covariance matrix for the oscilloscope response using a generalization of the techniques described in [23].

B. Impedance Calibration

We wish to calibrate the voltage the generator delivers to a specified load (usually 50 Ω) [13] at its 3.5-mm connector. However, the pulsed signal from our generator has significant energy above the single-mode cutoff frequency of the 3.5-mm connector (∼33 GHz), and the possibility of higher order modes propagating in the generator, adapters, and samplers used in the measurement must be considered. If the coupling between the fundamental mode and higher-order modes were known, along with the reflection coefficient of all the modes at each junction, a multiport model of the measurement system could be constructed, and the effects of the higher-order modes could be calibrated in a systematic way. As this information is not available, we take a different approach. We measure the (fundamental mode) scattering parameters of the 3.5–1.0-mm adapters directly up to 33 GHz, and extend these scattering-parameter measurements to 110 GHz with an empirical single-mode model. We also measure the reflection coefficient of the generator directly to 33 GHz and extend this reflection coefficient to 110 GHz using measurements of the reflection coefficient of the generator plus adapter (performed at the 1.0-mm reference plane).

When measuring the reflection coefficient of the generator, the generator circuit is biased to the post transition state. Other considerations are described in [13]. All the coaxial measurements were calibrated using the techniques in [29] with uncertainty analysis following the covariance-based techniques in [15, Sec. 6.1]. In Section V, we describe our methodology for quantifying variations due to high-order modes and other uncontrolled or unmodeled effects.

C. System Response

Our oscilloscope response measurements and scattering-parameter measurements are on a 200-MHz grid from dc to 110 GHz. Based on these measurements, we estimate the response of the oscilloscope and the adapters at the 3.5-mm reference plane in Fig. 2, accounting for the response of the sampler and all of the (fundamental mode) mismatch corrections of the oscilloscope, adapters, and generator to 110 GHz [13]. Finally, we calculate the covariance matrix associated with the response of the oscilloscope and the mismatch corrections. This covariance matrix will be used in our uncertainty analysis in Section VI.

In principle, dividing the measured waveform spectrum by the system's frequency response yields the spectrum of the voltage waveform that the generator supplies in the fundamental coaxial mode of its 3.5-mm connector to a perfect 50-Ω load. As is well known, this naïve deconvolution strategy is generally ill-posed, leading to time-domain results with greatly amplified noise. We discuss our regularized deconvolution procedure in Section IV.

IV. Waveform Deconvolution

Deconvolution of step-like waveforms using a DFT is complicated by boundary effects such as severe ringing near the boundary discontinuity (e.g., see [30] and the references therein). We use a ramp subtraction routine that is described in the Appendix to reduce these effects. Furthermore, deconvolution of our data is an ill-posed problem [17], [31]–[34] and requires regularization to obtain a meaningful result. We perform regularized deconvolution for each averaged waveform $\mathbf{y}$ using a Tikhonov regularization with a standard smoothness penalty defined by the discretized second-difference operator $\mathbf{l}$ and regularization parameter λ. That is, for a given λ, we obtain the reconstructed waveform $\mathbf{x}_\lambda$ from

$$\Delta\mathbf{x}_\lambda = \Im^{-1}\mathbf{A}_\lambda^{-1}\Im\Delta\mathbf{y} \tag{2}$$

where

$$\mathbf{A}_\lambda^{-1} = \operatorname{diag}\left(\frac{\bar{\mathbf{A}}}{|\mathbf{A}|^2 + \lambda^2|\mathbf{L}|^2}\right). \tag{3}$$

In (2), $\Im$ denotes the DFT matrix, $\Im^{-1}$ denotes its inverse, $\mathbf{A}$ and $\mathbf{L}$ denote the frequency-domain matrix representation of the system impulse response function and the second-difference operator, and $\overline{\mathbf{A}}$ denotes the complex conjugate of $\mathbf{A}$. The variables $\Delta\mathbf{x}_\lambda$ and $\Delta\mathbf{y}$ refer to "ramp-subtracted" waveforms. The ramps are different for $\mathbf{x}_\lambda$ and $\mathbf{y}$ but are known and described in the Appendix [specifically (31) and (33)]. In writing this solution, we have used the property that $\mathbf{A}$ and $\mathbf{L}$ are diagonal matrices. Note that subject to elementary algebra, (2) and (3) are identical to [34, eqs. (6)–(10)]. However, our parameter selection algorithm is different.

Early work in regularized deconvolution applied to waveform metrology used subjective methods for determining the regularization parameter [34]. Later work [17] argued that the parameter selection procedure should be automated based on knowledge of the noise in the measurement system. A review of

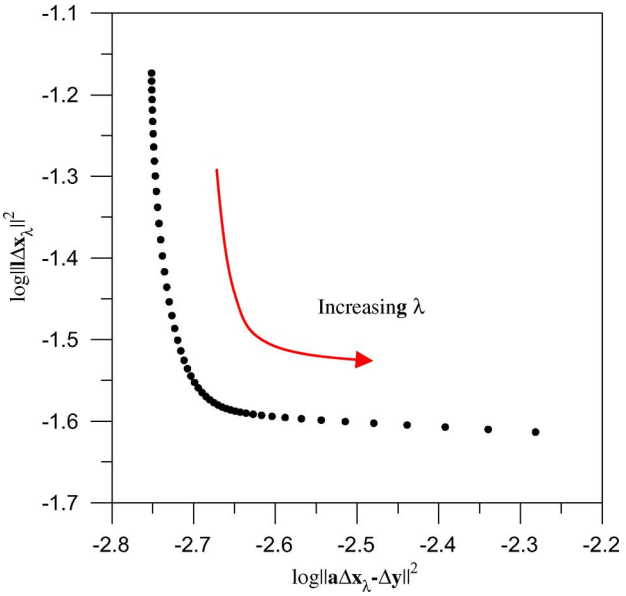

Fig. 3. (Dots) Typical "L-curve" used to find the regularization parameter λ^* at the point with maximum curvature.

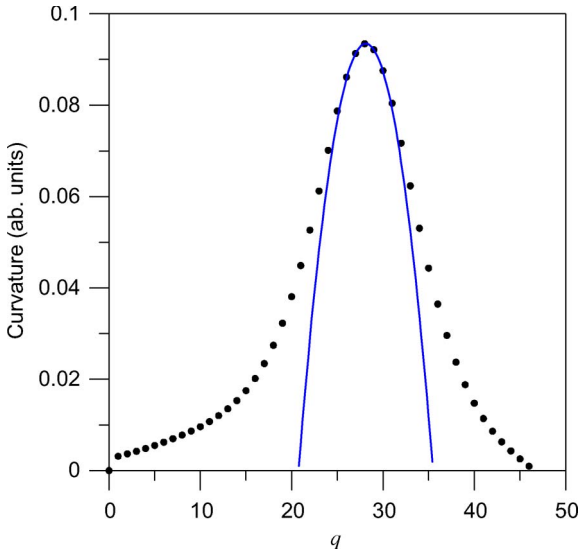

Fig. 4. (Dots) Curvature of L-curve. (Solid curve) Parabolic fit near maximum. The fit is used to estimate the regularization parameter λ^* and its uncertainty.

different methods for parameter selection can be found in [32, Ch. 7]. We use the heuristic "L-curve" method advocated in [32]. We choose the regularization parameter that balances the least squares error $\|\mathbf{a}\Delta\mathbf{x}_\lambda - \Delta\mathbf{y}\|^2$ and the smoothness penalty $\|\mathbf{l}\Delta\mathbf{x}_\lambda\|^2$. We select $\lambda = \lambda^*$ that maximizes the curvature in the L-curve shown in Fig. 3. This maximum is found by parameterizing λ as follows:

$$\lambda = \lambda(q) = \lambda_0 10^{qc}$$

where q is an integer, and λ_0 and c are constants chosen so that $\lambda(q)$ spans a reasonable range for inspecting the L-curve. We plot the curvature of the L-curve as a function of q in Fig. 4. We then fit the curvature in the region near the maximum with a parabola. The λ corresponding to the maximum of the parabola is λ^*.

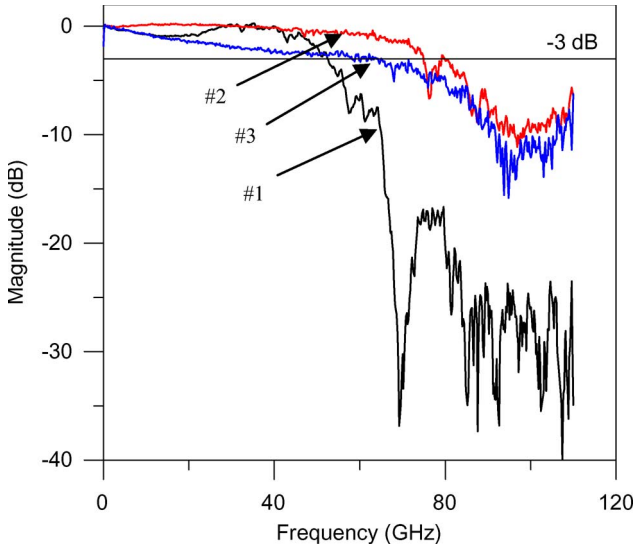

Fig. 5. Response magnitude for the three oscilloscope samplers used in this paper.

V. Input Signal Estimate

We vary our measurement system by use of different adapters and samplers and combine measurements taken with different system configurations to characterize the reproducibility uncertainty in our waveform calibration. For example, differently constructed adapters and oscilloscope samplers may introduce variations due to high-order modes, which, in turn, contribute to the uncertainty in the calibration of the response function of our measurement system. We use three 3.5–1.0-mm adapters (labeled B, R, and G) and three samplers (labeled 1, 2, and 3), giving a total of $I = 9$ possible measurement configurations. The 3.5–1.0-mm adapters, which are not commercially available, are constructed from two or three adapters with 2.4- and/or 1.85-mm coaxial connectors at the intermediate interfaces. We expect that the reflection coefficient for the generator and samplers, and the scattering parameters for the adapters will be different for high-order modes than for the fundamental mode. The waveform variations resulting from the different configurations are characterized by the reproducibility uncertainty that we estimate in Section VI. If the pulse generator has sufficient bandwidth to excite high-order modes, the variation in our measurements will include the uncertainty due to their excitation. If the pulse generator does not have enough bandwidth to excite high-order modes, variations in our measurements will not be due to their excitation, and our single-mode characterization will be sufficient.

By measuring waveforms using measurement systems with markedly different response functions, we sample our ability to characterize such differences and to remove their effect on the waveform calibration. We use three different sampler models from the same manufacturer. The magnitude of their frequency-domain response function is shown in Fig. 5. The response of sampler 1 is peaked at about 40 GHz and rolls off rapidly to a -3 dB point around 50 GHz and exhibits a deep notch at about 70 GHz. The response of sampler 2 is fairly flat up to about 70 GHz, with a notch roughly 4 dB deep near 75 GHz. The response of sampler 3 rolls off roughly monotonically, achieving -3 dB around 60 GHz.

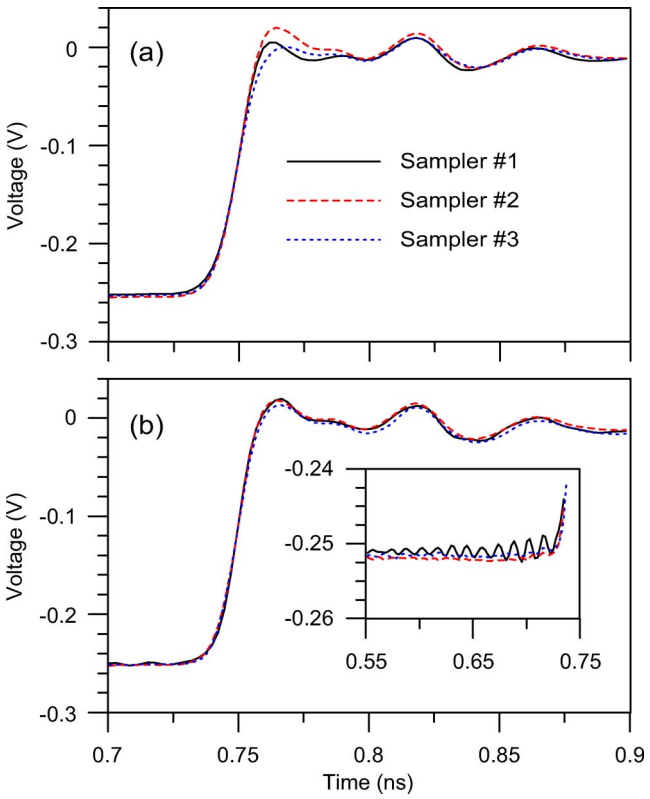

Fig. 6. Closeup of the pulse transition, as measured with the three different samplers and the first set of measurements ($j = 1$) with the B adapter (a) before correction for the system response and (b) after correction. The measured pulses have been aligned in time at the 50% crossing level instant. Before correction the 10%–90% transition durations are 16.5, 15.7, and 17.7, and after correction, they are 14.6, 15.3, and 15.1 ps. The inset in (b) shows pretransition ringing in the reconstructed waveform from sampler 1 that is due to the deconvolution process.

The most obvious difference between measured waveforms occurs between measurements made with different samplers. A portion of the waveforms measured by use of the B adapter and samplers 1, 2, and 3, without deconvolution of the system response, are shown in Fig. 6(a). We show the same portion of the waveforms after deconvolution in Fig. 6(b). The most notable difference between the waveforms is the overshoot immediately after the transition. The peak difference between the three waveforms in the region between 0.7 and 0.8 ns decreases by about a factor of 3 after deconvolution. None of the reconstructed waveforms exhibit ringing due to the hard cutoff at 110 GHz. This is consistent with our observation that the pulse generator does not produce significant energy at these frequencies (see Fig. 10). On the other hand, the deconvolved waveform measured with sampler 1 does have some ringing visible at times before the transition [shown in the inset of Fig. 6(b)] at a frequency of about 77 GHz.

We averaged the measurements over the full set of adapter and sampler combinations and characterized variations in the measurements obtained with different adapters and samplers (after correction for their respective system response functions). Each measurement of the generator, with a given configuration, included $J = 4$ repeat measurements consisting of the $K = 100$ averaged waveform measurements. Between each of the four repeat measurements, the pulse generator, adapters, and oscilloscope were disconnected and reconnected, and the system was allowed to equilibrate for one-half hour before beginning the next repeat measurement. This disconnect/reconnect procedure is intended to determine uncertainties from connector repeatability and other short-term measurement and instrumentation errors. In all, we measured $I \times J = 36$ sets of $K = 100$ waveforms.

The 36 data sets were measured over the course of a few days, during which the standard deviation of the laboratory temperature was 1.0 °C. Because of temperature variations and long-term drift of our measurement system, the relative delay between the oscilloscope timebase and the generated pulse can drift significantly. In addition, we do not attempt to temporally align measurements that use different length adapters during the measurement process. Therefore, we numerically align the 50% reference level crossing time of each of the measured waveforms with the reference level crossing time of the first waveform to obtain a meaningful average and to quantify variations between the waveforms. This is achieved by the use of a frequency-domain technique with ramp subtraction (see the Appendix). All 36 waveforms are then averaged to find $\overline{\overline{\mathbf{x}}}$. The procedure for averaging and statistically quantifying variations between the measurements is described further in Section VI-B.

VI. Waveform Uncertainty Analysis

In this section, we describe the propagation of uncertainty through our measurement processes. As recommended by the International Organization for Standardization (ISO) Guide to the Expression of Uncertainty in Measurements [35], we categorize contributions to our uncertainty budget into two types, namely, type A and type B. Type A are those that are determined by statistical means based on repeated measurements. Type B are those that are determined in some other way, including scientific judgment based on all available information on the variability of the uncertainty source, as discussed in [35, Sec. 4.3.1].

A. Deconvolution Uncertainty

Following the techniques described in [15], [16], and [35], we use the first-order Taylor expansion for algorithms and procedures, as well as functions, as long as they are sufficiently linear and differentiable with respect to the sources of error. We refer to the above process of deconvolving the system response as a procedure $\mathcal{D} = \mathcal{D}(\mathbf{A}, \mathbf{y}, \lambda(q))$. We use a covariance-matrix-based approach for propagating the uncertainty in $\mathbf{A}$, $\mathbf{y}$, and $\lambda(q)$ through the deconvolution procedure.

We determine the sensitivity of the deconvolution procedure $\mathcal{D}$ to its various arguments (described in Section IV) by calculating the following Jacobians using a finite difference method:

$$\mathbf{J}_{\mathbf{A}} = \frac{\partial \mathcal{D}}{\partial \mathbf{A}}$$
$$\mathbf{J}_{\mathbf{y}} = \frac{\partial \mathcal{D}}{\partial \mathbf{y}}$$
$$\mathbf{J}_{q} = \frac{\partial \mathcal{D}}{\partial q}. \tag{4}$$

Note that $\mathbf{J}_{\mathbf{A}}$ and $\mathbf{J}_{\mathbf{y}}$ are matrices, while $\mathbf{J}_q$ is a column vector. Furthermore, all the derivatives are evaluated at $\lambda = \lambda^*$. The

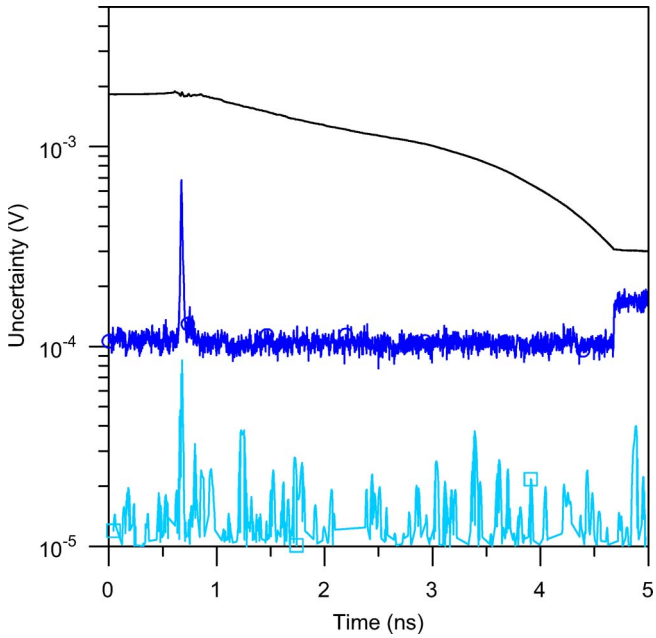

Fig. 7. Contributions to $\mathrm{diag}(\mathbf{\Sigma}_{\mathbf{x}_\lambda})$ in (5) from uncertainty in the system response function (top), the signal measurement (middle), and the regularization parameter (bottom).

covariance $\mathbf{\Sigma}_{\mathbf{x}_\lambda}$ in the estimated waveform is found using propagation of uncertainties [15], [16], [35] as follows:

$$\mathbf{\Sigma}_{\mathbf{x}_\lambda} = \mathbf{J}_\mathbf{A}\mathbf{\Sigma}_\mathbf{A}\mathbf{J}_\mathbf{A}^T + \mathbf{J}_\mathbf{y}\mathbf{\Sigma}_\mathbf{y}\mathbf{J}_\mathbf{y}^T + \mathbf{J}_q\sigma_q^2\mathbf{J}_q^T \tag{5}$$

where $\mathbf{\Sigma}_\mathbf{A}$ is the covariance matrix of the system response function in the time domain, and $\mathbf{\Sigma}_\mathbf{y}$ is the covariance matrix of the timebase-corrected mean waveform $\mathbf{y}$. The 1×1 matrix σ_q^2 is the squared uncertainty of the regularization parameter λ. We have verified, using Monte Carlo simulations, that the first-order Taylor series expansions used in (5) are valid approximations of the deconvolution uncertainty, given the range of dispersion characterized by $\mathbf{\Sigma}_\mathbf{A}$, $\mathbf{\Sigma}_\mathbf{y}$, and σ_q^2. We next describe the different terms to (5) in more detail.

1) System Response Covariance $\mathbf{\Sigma}_\mathbf{A}$: Details on how the covariance $\mathbf{\Sigma}_\mathbf{A}$ is calculated are given in [15] and [23]. This is a type B uncertainty component. The square root of the diagonal elements of $\mathbf{J}_\mathbf{A}\mathbf{\Sigma}_\mathbf{A}\mathbf{J}_\mathbf{A}^T$ are plotted as the top curve in Fig. 7. We observe that the primary contribution to the uncertainty of $\mathbf{x}_\lambda$ comes from the uncertainty in the convolution kernel a (i.e., the system response function) from which the discretized operators $\mathbf{a}$ and $\mathbf{A}$ are found. In the present measurement context, we find that this contribution to the uncertainty in $\mathbf{x}_\lambda$ decreases as a function of time. We attribute this to the fact that a large component of the uncertainty in deconvolution arising from uncertainty in the underlying convolution kernel can itself be represented as some convolution applied to the measured waveform.

To see this, recall that the deconvolution operator, even with regularization, is diagonal in the frequency domain. Assuming for the moment that there are no cross-frequency correlations, one can verify that the Jacobian operators required for uncertainty propagation with respect to the system response function (i.e., the convolution kernel $\mathbf{a}$) will preserve this diagonal structure in the frequency domain. Now, it is a mathematical fact that an operator is convolutional in the time domain if and only if it is diagonal in the frequency domain. It follows that the time-domain contribution to the uncertainty arising from the underlying convolution kernel is itself convolutional. This argument ignores cross-frequency correlations. In practice, we do not ignore these correlations but rather propagate them faithfully through our analysis. Nevertheless, assuming a large diagonal component to the deconvolution kernel uncertainty, by this argument, we can conclude that some correspondingly large contribution to the uncertainty in the calibrated waveform has a convolutional structure in the time domain. Next, we recall that the uncertainty in the system response function (i.e., our convolution kernel $\mathbf{a}$) is largest at low frequencies due to the corresponding relatively large uncertainty at these frequencies in the electro-optic calibration of the photodiode. In the time domain, this low-frequency uncertainty manifests as a "time-domain uncertainty convolution kernel" with a relatively long time constant. Applying this kernel to a step-like waveform that transitions to zero, it follows that there should exist a corresponding decay in the uncertainty in the estimate of $\mathbf{x}_\lambda$. Note that the same argument implies that this component of uncertainty grows if the waveform transitions to a nonzero constant, as we have observed in other measurement situations.

2) Signal Covariance $\mathbf{\Sigma}_\mathbf{y}$: This is the covariance of the measured waveform after correction for timebase errors. The matrix is estimated by the sample covariance as

$$(\mathbf{\Sigma}_\mathbf{y})_{m,n} = \frac{1}{K(K-1)}\sum_{k=1}^{K}(y_{k,m} - \overline{y}_m)(y_{k,n} - \overline{y}_n) \tag{6}$$

where $m,\ n = 1, \ldots, 2048$, and $K = 100$. This is a type A uncertainty component. The square roots of the diagonal elements of $\mathbf{J}_\mathbf{y}\mathbf{\Sigma}_\mathbf{y}\mathbf{J}_\mathbf{y}^T$ are represented by the middle curve plotted in Fig. 7. The broad background in this contribution is due to noise in the measurement system, while the bump occurring at the pulse transition is probably due to residual jitter (about 450 fs) that is contributed by the prescalers in Fig. 2, the pulse generator, and the firing of the samplers. The discontinuity at about 4.8 ns is a boundary effect due to the time translation in the deconvolution process, as is the level region in the curve corresponding to $\mathbf{J}_\mathbf{A}\mathbf{\Sigma}_\mathbf{A}\mathbf{J}_\mathbf{A}^T$. These aberrations in the uncertainty estimate occur because of the periodic nature of the DFT. Such boundary effects are common in deconvolution problems [30]. Despite our best efforts to minimize this effect, it still appears, but at a level of less than 0.15% (approximately 0.36 mV/250 mV). We intend to explore this effect further in the future.

3) Regularization Parameter Variance σ_q^2: The 1×1 matrix σ_q^2 is the squared uncertainty in the parameter q of $\lambda(q)$. Although there is no "true" value for $\lambda^* = \lambda(q^*)$, there is a range of λ around λ^* over which $\mathbf{x}_\lambda$ is reasonably stable. We estimate σ_q as the half width of a parabolic fit to the curve shown in Fig. 5 at half of its maximum. This term generally has negligible contribution compared to the preceding two terms. This is a type B uncertainty component.

4) Total Deconvolution Correlation Matrix: The total deconvolution uncertainty is dominated by the uncertainty in

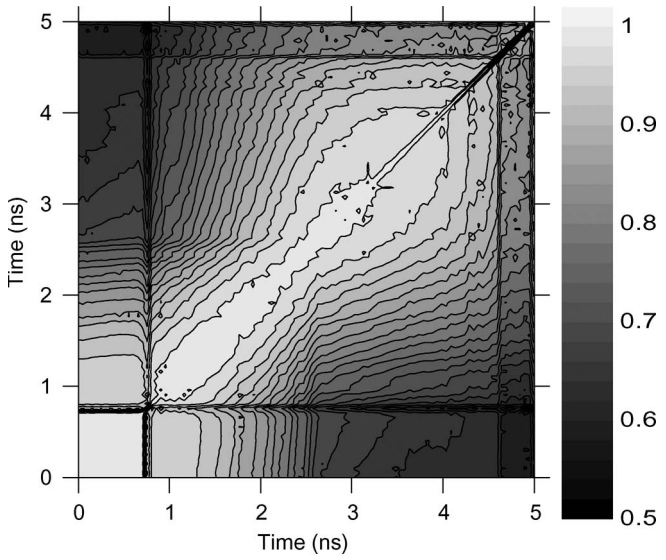

Fig. 8. Values of correlation matrix corresponding to $\mathbf{\Sigma}_{\mathbf{x}_\lambda}$ in (5).

the oscilloscope calibration, which, in turn, is dominated by uncertainty in the calibration of the photodiode that is used to calibrate the oscilloscope. Fig. 8 shows a plot of the 2048 $\times$ 2048 correlation matrix described as follows:

$$(\mathbf{R}_{\mathbf{x}_\lambda})_{m,n} = \frac{(\mathbf{\Sigma}_{\mathbf{x}_\lambda})_{m,n}}{\sqrt{(\mathbf{\Sigma}_{\mathbf{x}_\lambda})_{m,m}}\sqrt{(\mathbf{\Sigma}_{\mathbf{x}_\lambda})_{n,n}}}. \tag{7}$$

Fig. 8 shows that the uncertainties in the deconvolution process are highly correlated due to uncertainties in the low-frequency calibration and gain of the oscilloscope.

B. Repeatability and Reproducibility

To characterize our ability to calibrate our measurements, we use a type A evaluation and separate the components of repeatability (the variations observed while attempting to keep the measurement conditions the same) and the reproducibility (the variation in measurements due to specific changes in the measurement apparatus while attempting to keep all other measurement conditions the same). We follow a procedure similar to that described in [36, Ch. 9] and in [37, Sec. 15.2].

The mean waveform $\overline{\mathbf{x}}^i$ for the ith oscilloscope and adapter measurement configuration ($i = 1, \ldots, I$, where $I = 9$, and dropping the λ^* subscript for clarity) is then calculated by averaging over the $J = 4$ repeated (time aligned) measurements $\mathbf{x}_j^i$ performed within a given oscilloscope and adapter measurement configuration as

$$\overline{\mathbf{x}}^i = \frac{1}{J}\sum_{j=1}^{J} \mathbf{x}_j^i. \tag{8}$$

Repeatability uncertainty within a measurement set, including variations due to connector repeatability, is described by the following sample covariance matrix:

$$\mathbf{S}_{\mathrm{r}}^i = \frac{1}{J-1}\sum_{j=1}^{J} \left(\mathbf{x}_j^i - \overline{\mathbf{x}}^i\right)\left(\mathbf{x}_j^i - \overline{\mathbf{x}}^i\right)^T. \tag{9}$$

We assume that the repeatability for each measurement configuration is the same and pool within-measurement repeatability by averaging over all the measurement sets as follows:

$$\mathbf{S}_{\mathrm{r}} = \frac{1}{I}\sum_{i=1}^{I} \left(\mathbf{S}_{\mathrm{r}}^i\right). \tag{10}$$

We estimate the reproducibility covariance matrix $\mathbf{S}_R$ as

$$\mathbf{S}_{\mathrm{R}} = \frac{1}{J}(\mathbf{S}_{\mathrm{rms}} - \mathbf{S}_{\mathrm{r}}) \tag{11}$$

where $\mathbf{S}_{\mathrm{rms}}$ is the mean square variation between the $I = 9$ measurement configurations, i.e.,

$$\mathbf{S}_{\mathrm{rms}} = \frac{J}{I-1}\sum_{i=1}^{I} (\overline{\mathbf{x}}^i - \overline{\overline{\mathbf{x}}})(\overline{\mathbf{x}}^i - \overline{\overline{\mathbf{x}}})^T \tag{12}$$

and

$$\overline{\overline{\mathbf{x}}} = \frac{1}{I}\sum_{i=1}^{I} \overline{\mathbf{x}}^i \tag{13}$$

is the average of the means $\overline{\mathbf{x}}^i$, averaged over all I measurement configurations. $\overline{\overline{\mathbf{x}}}$ is the average over all 36 measurements.

For $\mathbf{S}_{\mathrm{R}}$ to be a covariance matrix, it must be nonnegative definite. That is, $\mathbf{z}^T\mathbf{S}_{\mathrm{R}}\mathbf{z} \geq 0$ for every $N \times 1$ real vector $\mathbf{z}$. This can be verified by showing that all the eigenvalues of $\mathbf{S}_{\mathrm{R}}$ are nonnegative. If a negative eigenvalue is found, we set $\mathbf{S}_{\mathrm{R}}$ equal to zero. In practice, however, this computationally intensive test is not necessary when $\mathbf{S}_{\mathrm{R}}$ is projected to a much smaller dimension such as the 1-D and 2-D pulse metrics discussed in this paper. For example, in calculating the uncertainty of the pulse amplitude, $\mathbf{S}_{\mathrm{R}}$ is projected to a scalar, and we set the resulting projection to zero if it is negative. We find that the projection is greater than zero for the generator and all the pulse parameters reported in this paper. It should be noted that we are not interested in the inference of the individual off-diagonal elements of the full 2048 $\times$ 2048 covariance matrix, which are estimated based on a relatively small number of measurements [15]. As we will see in Section VII, the number of measurements taken here is sufficient for estimating the uncertainties of the low-dimensional waveform metrics discussed in this paper.

C. Timing Errors

We find that the residual jitter after correction for timebase errors is about 450 fs, which has a negligible effect on the measurement of pulses with a roughly 15-ps transition duration. We have analyzed the uncertainty associated with the timebase correction algorithms and have found it to be negligible for this application [38]. We also find that the drift within the 100-sweep data set for this pulse generator is negligible. We conclude that with our typical laboratory stability, we do not need to include uncertainty terms for these potential effects in the present work.

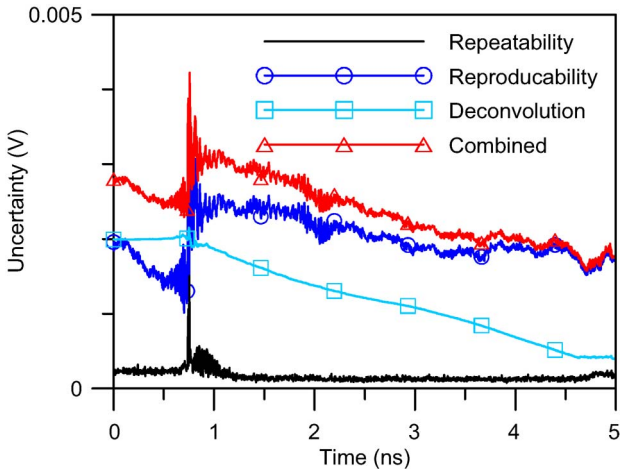

Fig. 9. Combined uncertainty from (14) and the various components contributing to it.

D. Combining Uncertainties

Equations (5), (10), and (11) evaluate the individual contributions of various sources of uncertainty. We combine the uncertainties using the full covariance matrices to find the standard uncertainty of the averaged waveform vector $\overline{\overline{\mathbf{x}}}$ using

$$\mathbf{S}_{\mathrm{c}} = \frac{\mathbf{S}_{\mathrm{r}}}{J} + \mathbf{S}_{\mathrm{R}} + \overline{\mathbf{\Sigma}}_{\mathbf{x}_\lambda} \tag{14}$$

where $\overline{\mathbf{\Sigma}}_{\mathbf{x}_\lambda}$ is the covariance matrix for the systematic uncertainty pooled over all $I = 9$ measurement configurations. The diagonal elements of the covariance matrices in (14) are plotted in Fig. 9.

VII. Pulse Parameters

In this section, we use the procedures that were described in [14] for calculating pulse parameters and give a detailed description of how we calculate the uncertainties for the measurements described in this paper. We write all procedures in terms of matrix operations on the averaged waveform vector $\overline{\overline{\mathbf{x}}}$ and its covariance, and thus, we refer to this method as the waveform method. In the last part of this section, we also describe similar but somewhat more traditional procedures to calculate the pulse parameters from the individual (unaveraged) waveforms. We then conduct the uncertainty analysis on the pulse parameters themselves. We refer to this approach as the parametric method. The results of the two methods are given in Table I. Although the procedure $\mathcal{P} = \mathcal{P}(\mathbf{x})$ for extracting a pulse parameter from the waveform might be expected to be nonlinear, it was also shown in [14] that the operations are sufficiently linear that a first-order Taylor expansion gives adequate accuracy for our uncertainty estimate. We show here that the method is also locally linear in the sense that

$$\mathcal{P}(\overline{\overline{\mathbf{x}}}) \approx \frac{1}{IJ}\sum_{i,j}\mathcal{P}\left(\mathbf{x}_j^i\right)$$

within the uncertainty of our experiment, thereby validating our procedure for combining measurements from different instruments.

A. Extracting Pulse Parameters: Waveform Method

We first cluster the individual time samples of the estimated pulse $\overline{\overline{\mathbf{x}}}$ into the initial voltage state $S1$ before the step and the final voltage state $S2$ after the step using the "k-means" method, described in [39] and [40]. The samples are thereby sorted by their distance from a particular cluster mean. Each state level is determined through the *shorth*, that is, the mean of the data contained in the shortest interval that contains half the data in the cluster corresponding to that state [41].

The vector $\mathbf{L} = (L_1, L_2)^T$, representing the state levels, can be expressed as a linear transformation of $\overline{\overline{x}}$. That is

$$\mathbf{L} = \mathbf{H}_{\mathbf{L}}\overline{\overline{\mathbf{x}}} \tag{15}$$

where $\mathbf{H}_{\mathbf{L}}$ is a 2×2048 matrix. The jth element of the first row of $\mathbf{H}_{\mathbf{L}}$ is

$$\begin{cases} 1/N_1, & \text{if } \overline{\overline{x}}_j \text{ is used in the calculation of state } S1 \\ 0, & \text{if } \overline{\overline{x}}_j \text{ is not used in the calculation of state } S1. \end{cases} \tag{16}$$

The jth element of the second row of $\mathbf{H}_{\mathbf{L}}$ is

$$\begin{cases} 1/N_2, & \text{if } \overline{\overline{x}}_j \text{ is used in the calculation of state } S2 \\ 0, & \text{if } \overline{\overline{x}}_j \text{ is not used in the calculation of state } S2. \end{cases} \tag{17}$$

Here, N_1 and N_2 are the number of points in the clusters describing states $S1$ and $S2$, respectively, and $N_1 + N_2 = 2048$.

We find the pulse amplitude $A = L_2 - L_1$ from the linear transformation of the vector $\mathbf{L}$ as

$$A = \mathbf{J}_{\mathrm{amp-L}}\mathbf{L} \tag{18}$$

where $\mathbf{J}_{\mathrm{amp-L}} = (-1 \quad 1)$. A similar transformation for calculating the pulse transition duration is described in [14].

B. Pulse Parameter Uncertainties: Waveform Method

Writing the pulse parameter extraction procedure as a function of the waveform vector, that is, $\mathcal{P} = \mathcal{P}(\mathbf{x})$, allows us to use the standard propagation of uncertainty techniques to estimate the uncertainty in our estimated pulse parameters. The sensitivity of the pulse parameter to a given waveform is found by calculating the following Jacobian:

$$\mathbf{J}_{\mathcal{P}} = \frac{\partial \mathcal{P}}{\partial \mathbf{x}}. \tag{19}$$

Since the first-order Taylor-series expansion gives adequate accuracy, the Jacobian is simply the matrix used to transform between the waveform vector and the pulse parameter. For example, the pulse amplitude Jacobian $\mathbf{J}_{\mathrm{amp}} = \mathbf{J}_{\mathrm{amp-L}}\mathbf{H}_{\mathbf{L}}$.

The deconvolution-related uncertainties given in Table I are found by using propagation of uncertainties as

$$u_{\mathcal{P}} = \sqrt{\mathbf{J}_{\mathcal{P}}\overline{\mathbf{\Sigma}}_{\mathbf{x}_\lambda}\mathbf{J}_{\mathcal{P}}^T}. \tag{20}$$

Note that $\mathbf{J}_{\mathcal{P}}$ is a row vector, and therefore, the transformation inside the radical of (20) gives a scalar quantity. The

TABLE I
SOME PULSE PARAMETERS AND THEIR UNCERTAINTIES CALCULATED USING THE WAVEFORM AND PARAMETRIC METHODS DESCRIBED IN SECTION VII

	10 % – 90 % transition duration (ps)		20 % – 80 % transition duration (ps)		Amplitude (mV)	
	Waveform method	Parametric method	Waveform method	Parametric method	Waveform method	Parametric method
Mean value	14.89	14.90	9.86	9.88	247.84	247.80
Repeatability within each measurement configuration ($J = 4$)	0.10	0.11	0.07	0.06	0.4	0.2
rms variation between each measurement configuration ($I = 9$)*	0.86	0.90	0.70	0.71	1.4	1.6
Reproducibility between each measurement configuration ($I = 9$)	0.4	0.4	0.4	0.3	0.7	0.7
Uncertainty propagated through deconvolution**	0.14	--	0.1	--	1.6	--
Combined standard uncertainty, U_c	0.45	0.47	0.36	0.37	1.7	1.7
Expanded uncertainty (95 % confidence), kU_c	1.01	1.01	0.82	0.82	3.4	3.5
Degrees of freedom ν from Welch-Satterthwaite formula (dimensionless, used to find k)	10	10	10	10	100	89

*Used only in (11) for calculating reproducibility and is not summed directly with other components.
**The deconvolution uncertainties for the waveform method were used for the single-parameter method.

repeatability- and reproducibility-related uncertainties shown in Table I are derived similarly by their respective covariance matrices, i.e.,

$$u_{\mathcal{P},\mathrm{r}} = \sqrt{\mathbf{J}_{\mathcal{P}}\mathbf{S}_{\mathrm{r}}\mathbf{J}_{\mathcal{P}}^{T}} \tag{21}$$

$$u_{\mathcal{P},\mathrm{R}} = \sqrt{\mathbf{J}_{\mathcal{P}}\mathbf{S}_{\mathrm{R}}\mathbf{J}_{\mathcal{P}}^{T}}. \tag{22}$$

As shown in Table I, the reproducibility is the dominant source of uncertainty in the estimated transition durations, while the deconvolution uncertainty is the dominant contribution in the uncertainty in the amplitude estimate.

C. Combining Uncertainties

Finally, the combined uncertainty in the pulse parameter is found from the combined covariance matrix $\mathbf{S}_c$ as

$$U_{\mathcal{P}} = \sqrt{\mathbf{J}_{\mathcal{P}}\mathbf{S}_{\mathrm{c}}\mathbf{J}_{\mathcal{P}}^{T}}. \tag{23}$$

To find the expanded uncertainty $kU_{\mathcal{P}}$ (95% confidence interval), we use the individual contributions to the uncertainty in the pulse parameter in the Welch–Satterthwaite formula [35] and calculate the number of degrees of freedom ν. The factor k is the appropriate t-table value with ν degrees of freedom.

D. Parametric Method

To demonstrate the validity (and linearity) of our approach, we also use the more traditional approach to calculate the pulse parameter $\mathcal{P}$ from each waveform vector $\mathbf{x}_j^i$ individually using the same algorithm as above. By using $\mathcal{P}$ instead of $\mathbf{x}$ in (8) and (13), we calculate the average parameter $\overline{\overline{\mathcal{P}}}$. By using $\mathcal{P}$ instead of $\mathbf{x}$ in (9) and (12), we also calculate the within-set repeatability and rms between-sets variation of the parameter. We then calculate the pooled repeatability, the reproducibility, and the combined uncertainty using analogous versions of (10), (11), and (14), respectively. Note that the parametric method does not require waveform alignment before averaging.

E. Discussion

The pulse parameters in Table I agree to 0.2% or less, which exceeds the number of significant digits of our calibration. This validates our method of averaging the waveforms and demonstrates the algorithms, given in [14], in a practical application. Additionally, the uncertainties typically agree to within 20%, except for the repeatability of the amplitude. It is important to note that in the individual parameter approach, the repeatability and reproducibility are determined by 36 measurements of the scalar parameter. This number of measurements is usually adequate to obtain a high confidence in the result. In our waveform approach, we determine the 2048×2048 covariance matrices for repeatability and reproducibility with *only* 36 measurements so that the matrices are severely underdetermined. Nevertheless, we obtain good agreement in the uncertainties calculated by the two different methods. This is because the pulse parameter operators can be locally approximated by a linear projection of the 2048-D waveform vectors onto a 1-D space, effectively giving us 36 measurements of the scalar quantity.

The uncertainty in the pulse amplitude is dominated by deconvolution uncertainties, as can be seen by the relative magnitudes of the uncertainty contributions in Table I, as well as the number of degrees of freedom determined from the Welch–Satterthwaite formula (e.g., see [35, Sec. G.4]). In turn, the system response uncertainty is dominated by uncertainties that we trace back to the low-frequency uncertainty in the electro-optic calibration of the photodiode that we used to calibrate the oscilloscope. Reducing these low-frequency uncertainties is an area for further study.

The long tail in the combined uncertainty of Fig. 9 includes significant contributions from the deconvolution uncertainty and our measurement reproducibility. The uncertainties in the transition durations are dominated by variations between measurement configurations. While we can detect and quantify these variations, determining their physical source is a subject for further study. Possible sources of these variations include long-term variations in the measurement system or the generator, temperature effects, uncalibrated high-order mode effects, and artifacts in the deconvolution process, such as the ringing observed in the (corrected) measurements made by using sampler 1. This last effect might be part of a justification to reject the measurements made by sampler 1, although we do not attempt such justification here.

VIII. State-Level Vector

The scalar pulse parameters described in [3] are examples of scalar waveform metrics. Vector waveform metrics are also possible. Vector waveform metrics and their associated covariance matrices can give useful information regarding the variability in a set of waveform measurements and various sources of uncertainty. In this section, we apply our analysis to the following vector:

$$\mathbf{L} = (\, L_1 \quad L_2 \,)^T = (\, -0.25044 \quad -0.00260 \,)^T \tag{24}$$

whose elements are the state levels of our two-level pulse $\overline{\overline{\mathbf{x}}}$. We estimate the covariance matrix $\mathbf{\Sigma_L}$ of $\mathbf{L}$ from the combined covariance matrix as

$$\mathbf{\Sigma}_{\mathbf{L}\mathrm{c}} = \mathbf{H_L S}_{\mathrm{c}} \mathbf{H}_{\mathbf{L}}^T = \begin{bmatrix} 6.6 \times 10^{-6} & 3.8 \times 10^{-6} \\ 3.8 \times 10^{-6} & 3.8 \times 10^{-6} \end{bmatrix} \tag{25}$$

with a positive correlation of 0.7. We find the pulse amplitude uncertainty as

$$U_{\mathrm{amp}} = \mathbf{J}_{\mathrm{amp}-\mathbf{L}} \mathbf{\Sigma}_{\mathbf{L}\mathrm{c}} \mathbf{J}_{\mathrm{amp}-\mathbf{L}}^T \tag{26}$$

and obtain the same combined standard uncertainty as in (23) and Table I, i.e., 1.7 mV. However, if the correlations between the state levels are neglected, which we can do here by setting the off-diagonal elements to 0, the combined uncertainty becomes 3.2 mV, overestimating the amplitude uncertainty by nearly 90%. This example demonstrates the importance of including correlations in pulse waveform measurements.

We can look for the source of this correlation by calculating the contributions to the combined state-level covariance matrix due to deconvolution uncertainty, repeatability, and reproducibility as

$$\mathbf{\Sigma}_{\mathbf{L}\mathbf{x}_\lambda} = \mathbf{H_L} \overline{\mathbf{\Sigma}}_{\mathbf{x}_\lambda} \mathbf{H}_{\mathbf{L}}^T = \begin{bmatrix} 4.0 \times 10^{-6} & 1.1 \times 10^{-6} \\ 1.1 \times 10^{-6} & 5.6 \times 10^{-7} \end{bmatrix}$$

$$\mathbf{\Sigma}_{\mathbf{L}\mathrm{r}} = \mathbf{H_L S}_{\mathrm{r}} \mathbf{H}_{\mathbf{L}}^T = \begin{bmatrix} 1.9 \times 10^{-7} & 5.1 \times 10^{-10} \\ 5.1 \times 10^{-10} & 3.4 \times 10^{-9} \end{bmatrix}$$

$$\mathbf{\Sigma}_{\mathbf{L}\mathrm{R}} = \mathbf{H_L S}_{\mathrm{R}} \mathbf{H}_{\mathbf{L}}^T = \begin{bmatrix} 2.6 \times 10^{-6} & 2.7 \times 10^{-6} \\ 2.7 \times 10^{-6} & 3.3 \times 10^{-6} \end{bmatrix}. \tag{27}$$

The correlations are 0.7, 0.02, and 1.0, revealing high correlations in the uncertainty contributions from deconvolution and reproducibility. Further inspection of the waveforms reveals that measurements from the $I = 9$ measurement configurations are visibly shifted in voltage relative to each other. If we apply an offset to each of the measurements equal to the deviation of its high level from the mean high level of all the waveforms, the point-by-point uncertainty is greatly changed, but the entries in Table I and the mean state levels are unchanged. The adjusted state-level covariance matrix due to reproducibility is reduced to

$$\mathbf{\Sigma}'_{\mathbf{L}\mathrm{R}} = \mathbf{H_L S}'_{\mathrm{R}} \mathbf{H}_{\mathbf{L}}^T = \begin{bmatrix} 5.3 \times 10^{-7} & 3.4 \times 10^{-8} \\ 3.4 \times 10^{-8} & 2.2 \times 10^{-8} \end{bmatrix} \tag{28}$$

with a correlation of 0.3. Since the amplitude is invariant with respect to overall voltage shifts of the pulse, this transformation leaves the amplitude and the amplitude uncertainty unchanged, as can be verified using (14) and (26)–(28). The remaining state-level correlations are then dominated by the contribution from the deconvolution, and hence, the oscilloscope calibration uncertainty.

IX. Conclusion

In conclusion, we have presented an apparatus for measuring pulsed waveforms produced by a popular step-like pulse generator, and we have described our procedures for calibrating those measurements. We also described statistical procedures for characterizing how well these calibrations perform with respect to various changes in the measurement apparatus.

Our procedures are designed to fully calibrate the pulse generator and its output waveform. That is, we calibrate an equivalent-circuit model of the generator that can be used to calculate the voltage or current that the generator delivers to an arbitrary load at every time point in the measured waveform. The calibrated waveform vector and covariance matrices can be used to determine both scalar and vector waveform metrics and their uncertainty. As an example, we calculated pulse parameters using our approach and compared these with pulse parameters calculated using the more traditional procedure in which pulse parameters and their statistics are individually obtained from each measured waveform. We showed that the mean 10%–90% and 20%–80% transition durations, and the amplitude obtained from the two different methods are the same and that the uncertainties calculated by the two methods are, for practical purposes, the same, thus demonstrating the validity of our waveform-based approach. We further demonstrated a vector waveform metric, consisting of the two pulse-state levels, and showed the importance of correlations in the measurement uncertainty. We also showed that correlations in this vector can be used as a diagnostic tool.

Because we divide the calibration into two steps, i.e., 1) waveform calibration and 2) waveform metric calibration, our procedures can be used to calibrate arbitrary waveform metrics that can be determined, subject to the constraint that the desired metric computation admits a linear approximation. Furthermore, because we compensate for time and impedance errors, the waveform calibration procedures we

describe here can be extended to a wide variety of signals, including frequency combs [1] and multisines [2], and the relevant time- and frequency-domain waveform metrics pertaining to such signals can be calibrated completely. Certain applications may ultimately benefit from knowledge of the whole waveform that is calibrated by our procedures when, for example, the aberrations cannot easily or adequately be described by a few pulse parameters or other such metrics. The capability of calibrating the whole waveform, not just pulse parameters or other low-dimensional metrics, was not previously available. We anticipate that this new approach will open new avenues of waveform characterization to practitioners of high-speed signal metrology.

APPENDIX

In this appendix, we describe our procedure for computing the deconvolution of step-like waveforms. We model our measured waveform as the convolution of the waveform generator output and the response function of a linear time-invariant system subject to noise, i.e.,

$$y(t) = [a * x](t) + n(t).$$

Here, $y(t)$ is the measured waveform, $x(t)$ is the output of the waveform generator, $a(t)$ is the system response function, and $n(t)$ is a stationary and time-invariant noise process. The response function $a(t)$ is determined by a particular configuration of adapter and oscilloscope sampler. As discussed in Section III, the components of $\mathbf{a}$ are estimated along with their correlated uncertainties as a result of calibrations performed independently of the step waveform measurement of interest here. The estimation of $x(t)$ requires a deconvolution of the measurement. Furthermore, the functions of interest here [i.e., $x(t)$ and $y(t)$] are "step-like," as opposed to "impulse-like." Consequently, the values of the waveform at the two endpoints do not agree. As is well-known in waveform metrology, this adds an additional difficulty to standard deconvolution strategies. In part, this is due to the fact that the Fourier transform of a step-like waveform does not exist in the usual sense but must be understood as a generalized object (for a discussion, refer to [42, Ch. 3 and Appendix I]).

Deconvolution of step-like waveforms shares many of the same features as the closely related problem of numerical estimation of the Fourier transform of step-like waveforms. However, there is a fundamental difference between the two, which we elaborate upon here. As customary in the analysis of linear time-invariant systems, we make use of the fact that convolution and deconvolution operators are diagonal in the frequency domain [recall the Fourier transform convolution identity $[a * x](t) \leftrightarrow A(f)X(f)$]. Therefore, something akin to frequency-domain estimates of the functions $a(t)$ and $y(t)$ is required to facilitate the procedure. However, unlike the problem of estimating the Fourier transform $Y(f)$ from discretization of $y(t)$, the goal of our analysis is to estimate $x(t)$. This, combined with the linearity of the deconvolution, means that we are free to add and subtract terms as intermediate steps to facilitate the appropriate spectral transforms. In this appendix, we discuss a discretized deconvolution procedure. We do not attempt to estimate the spectrum of step-like waveforms.

Our approach is very similar to the "ramp-subtraction" method discussed by Nicolson [43] and Waldmeyer [44] in the context of spectral estimation, and by Paulter and Stafford [30] in the context of deconvolution. The primary distinction here is that we do not subtract a linear ramp, but rather a smoother function that can be designed to achieve quiescent levels before and after the transition.

We assume an equi-spaced discretization of time $t_n = n\Delta t$ for $n = 0, \ldots, N-1$. Recall that $a(t)$ is determined by independent adapter and oscilloscope calibrations. If these measurements naturally occur on different time scales from the step waveform measurement, then we assume that the response function has been interpolated to the measurement time grid. Thus, we have vectors[4] corresponding to measurements of the impulse response function (combined oscilloscope/adapter) and the step waveform on the same time grid, i.e.,

$$\mathbf{a} = a(t_m), \qquad m = 0, \ldots, M-1$$

$$\mathbf{y} = y(t_n), \qquad n = 0, \ldots, N-1.$$

The different lengths of the two time records merit discussion. As mentioned in Section II-B, we arrange the time interval of the step waveform measurement to be sufficiently long such that pre-transition and post-transition aberrations are negligible near the time boundaries. The idea is that, given initial and final values of the waveform, i.e., y_{init} and y_{final}, extension of the measured waveform $\mathbf{y}$ by these two constant values at either end of the time window accurately represents $y(t)$ outside the measurement window. The impulse response function within the limits of measurement accuracy and noise is assumed to be active for some finite time, i. e., $a(t)$ is nonzero for $0 < t < M\Delta t$, and $a(t) \approx 0$ for $t > M\Delta t$. Necessarily, $M < N$; otherwise, the claim that the measured step waveform $\mathbf{y}$ has settled near the time boundaries would be invalid. It is more desirable that $M \ll N$. Experimentally, this corresponds to a time buffer occurring between the dynamic region of the step waveform (transition instant and aberration intervals) and the boundaries of the measurement time interval. Again, these statements are all subject to the limits of measurement accuracy.

The time-discretized vectors $\mathbf{a}$ along with $\mathbf{y}$ and the settled state values $(y_{\text{init}}, y_{\text{final}})$ are the assumed data. We compute both a "standard" ramp waveform and the convolution of that waveform with the response vector $\mathbf{a}$. For the standard ramp function, we use a shifted and scaled error function erf as follows:

$$r_n = \operatorname{erf}\left(\frac{t_n - \tau}{\sigma}\right) \tag{29}$$

The choice of τ and σ are subject to the same constraints as the measured waveform $\mathbf{y}$, i.e., the transition occurs in the interior

[4]Note that there is a slight abuse of notation here. Sometimes $\mathbf{a}$ refers to a vector and other times it refers to a matrix form of convolution by that vector. Here, and in the following, the usage should be clear from context.

of the measured time window, and the waveform has settled to its initial and final values near the time-interval boundaries but are otherwise free parameters. With appropriate caveats (addressed below), the final estimation of $x(t)$ does not depend on τ and σ. Note that a linear ramp function, as used in [43], does not settle but is dynamic over the entire time record. This can cause problems as discussed in [30].

The convolution $\tilde{r} = a * r$ is computed as the following discrete sum:

$$\tilde{r}_n = \sum_{m=0}^{M} r(t_n - t_m)a(t_m). \tag{30}$$

A few points are worth noting.

1) The sum need not extend to negative values of m, as the response function is assumed to be causal; $a(t) = 0$ for $t \leq 0$.
2) There are no issues interpreting the sum for values $t_n - t_m < 0$, as $\mathbf{r}$ can be extended to those time values by (29).
3) The sum in (30) is computed in direct space at a computational cost $O(NM)$. It is common practice to compute convolutions via a fast Fourier transform (FFT) to decrease this cost. However, FFT implementation of a convolution has an implicit assumption of periodicity. The mismatch between periodicity and step waveforms is at the heart of the problem. Therefore, we compute (30) directly.

Next, we rescale the pair $\mathbf{r}$ and $\tilde{\mathbf{r}}$ to match the measurement $\mathbf{y}$ at the initial and final values as follows:

$$\begin{aligned} \tilde{\mathbf{r}} &\rightarrow h\tilde{\mathbf{r}} + (y_{\text{inital}} - h\tilde{r}_{\text{initial}}) \\ \mathbf{r} &\rightarrow h\mathbf{r} + (y_{\text{inital}} - h\tilde{r}_{\text{initial}})/\alpha \end{aligned} \tag{31}$$

with the scaling factors defined as

$$\begin{aligned} h &\equiv (y_{\text{final}} - y_{\text{inital}})/(\tilde{r}_{\text{final}} - \tilde{r}_{\text{inital}}) \\ \alpha &\equiv \sum a_n \end{aligned}$$

where $\tilde{r}_{\text{inital}}$ and $\tilde{r}_{\text{final}}$ are calculated before rescaling.

At this point, we have constructed a pair of ramps that are consistently related by (nonperiodic) convolution with the system response, $\tilde{\mathbf{r}} = \mathbf{ar}$. Additionally, subject to noise in the measurement $\mathbf{y}$, the vector $\mathbf{y} - \tilde{\mathbf{r}}$ is zero at both ends.

Returning to the deconvolution problem, we wish to find $\mathbf{x}$ such that $\mathbf{ax} = \mathbf{y}$. Recalling that $\mathbf{ar} = \tilde{\mathbf{r}}$, we can subtract it from both sides, i.e.,

$$\begin{aligned} \mathbf{ax} &= \mathbf{y} \\ \mathbf{a}\Delta\mathbf{x} &= \Delta\mathbf{y} \end{aligned} \tag{32}$$

where

$$\begin{aligned} \Delta\mathbf{y} &\equiv \mathbf{y} - \tilde{\mathbf{r}} \\ \Delta\mathbf{x} &\equiv \mathbf{x} - \mathbf{r}. \end{aligned} \tag{33}$$

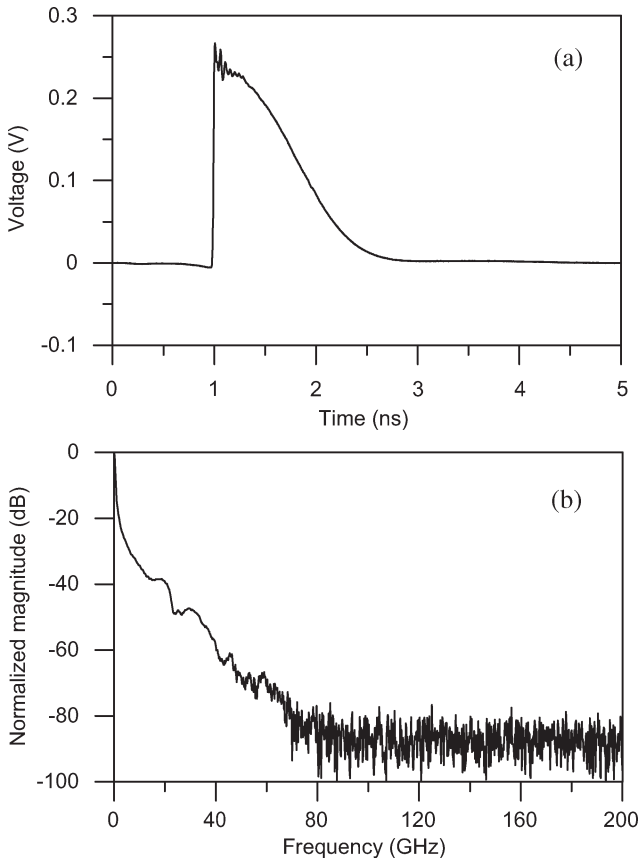

Fig. 10. (a) Ramp-subtracted waveform measured by the use of sampler 2. (b) Spectrum of the ramp-subtracted waveform. The Nyquist frequency is 204.8 GHz.

The point is that $\Delta\mathbf{y}$, as well as all derivatives, is zero at both ends, within the noise limits. In addition, to the extent that the transition region is well separated from the interval boundaries, it is also acceptable within measurement error to replace the convolution with a periodized convolution matrix. The deconvolution problem is then diagonalized by the DFT matrix. In this form, (32) can be restated in the following convenient form:

$$\mathbf{A}\Im\Delta\mathbf{x} = \Im\Delta\mathbf{y} \tag{34}$$

where $\Im$ denotes the DFT matrix, and $\mathbf{A}$ denotes the frequency-domain matrix representation of the system impulse response function. The ramp-subtracted waveform $\Delta\mathbf{y}$, corresponding to a measurement with sampler 2 and the B adapter, is shown in Fig. 10.

Finally, as all measurements are subject to uncertainty, some form of regularization is required. As discussed in Section IV, we choose a Tikhonov regularization procedure and select the regularization parameter using the "L-curve" method [32]. We choose a periodized second-difference operator as our penalty metric. As this matrix is also circulant, it is simultaneously diagonalized by the DFT. The rest of the deconvolution, i.e., parameter selection and application of the regularized inversion, are performed as described in Section III to solve for

$\Delta\mathbf{x}_\lambda$. By reversing the steps in (32), we estimate the regularized deconvolution $\mathbf{x}_\lambda$ as

$$\Im\Delta\mathbf{x}_\lambda = \mathbf{A}_\lambda^{-1}\Im\Delta\mathbf{y}$$
$$\Delta\mathbf{x}_\lambda = \Im^{-1}\mathbf{A}_\lambda^{-1}\Im\Delta\mathbf{y} \tag{35}$$

where

$$\mathbf{x}_\lambda \equiv \Delta\mathbf{x}_\lambda + \mathbf{r} \tag{36}$$

and $\mathbf{A}_\lambda^{-1}$ is given in (3). The idea is that the ramp functions $\mathbf{r}$ and $\tilde{\mathbf{r}}$ have been added and subtracted in such a way as to have no net effect. By performing some algebra, we find that this is true to the extent that

$$\mathbf{r} = \Im^{-1}\mathbf{A}_\lambda^{-1}\Im\tilde{\mathbf{r}} = \Im^{-1}\mathbf{A}_\lambda^{-1}\Im(\mathbf{ar}) = \mathbf{a}_\lambda^{-1}\tilde{\mathbf{r}}. \tag{37}$$

Informally speaking, $\mathbf{A}_\lambda^{-1}$ is designed to invert $\mathbf{A}$ on a "low-frequency subspace." Thus, it is desirable to set the steepness of the ramp $r(t)$ [i.e., the parameter σ in (29)] to be much less than the steepness of the measured waveform y. We verify (37) as a diagnostic for our procedure.

REFERENCES

[1] H. C. Reader, D. F. Williams, P. D. Hale, and T. S. Clement, "Characterization of a 50 GHz comb generator," *IEEE Trans. Microw. Theory Tech.*, vol. 56, no. 2, pp. 515–521, Feb. 2008.

[2] K. A. Remley, P. D. Hale, D. I. Bergman, and D. Keenan, "Comparison of multisine measurements from instrumentation capable of nonlinear system characterization," in *66th ARFTG Conf. Dig.*, Dec. 2005, pp. 34–43.

[3] *IEEE Standard on Transitions, Pulses, and Related Waveforms*, 2003, IEEE Std. 181-2003.

[4] N. G. Paulter, A. J. A. Smith, D. R. Larson, T. M. Souders, and A. G. Roddie, "NIST–NPL interlaboratory pulse measurement comparison," *IEEE Trans. Instrum. Meas.*, vol. 52, no. 6, pp. 1825–1833, Dec. 2003.

[5] M. Bieler, S. Seitz, M. Spitzer, G. Hein, K. Pierz, U. Siegner, M. A. Basu, A. J. A. Smith, and M. R. Harper, "Rise-time calibration of 50-GHz sampling oscilloscopes: Intercomparison between PTB and NPL," *IEEE Trans. Instrum. Meas.*, vol. 56, no. 2, pp. 266–270, Apr. 2007.

[6] T. M. Souders, J. Andrews, A. Caravone, J. P. Deyst, C. Duff, and S. Nabboicheck, "A pulse measurement intercomparison," *IEEE Trans. Instrum. Meas.*, vol. 47, no. 5, pp. 1031–1036, Oct. 1998.

[7] J. R. Andrews, *Comparison of Ultra-Fast Risetime of 18 and 50 GHz Sampling Oscilloscopes (Updated to Include New Instruments Introduced in 2000)*, Apr. 2001, Picosecond Pulse Labs. Application Note AN-2d.

[8] *40 Gb/s and Return-to-Zero Measurements Using the Agilent 86100A Infinium DCA*, Nov. 2001, Agilent Technol. Product Note 86100-3.

[9] *Effect of Bandwidth on RZ Signals*, Feb. 2003, SHF Commun. Technol. AG. Application Note AN-RZMEAS-1.

[10] *Utilizing DSP to Optimize Real-Time Oscilloscope/Probe System Performance*, Jun. 2007, Tektronix. Application Note.

[11] N. G. Paulter and D. R. Larson, "Pulse parameter uncertainty analysis," *Metrologia*, vol. 39, no. 2, pp. 143–155, Apr. 2002.

[12] D. C. DeGroot, P. D. Hale, M. Vanden Bosche, F. Verbeyst, and J. Verspecht, "Analysis of interconnection networks and mismatch in the nose-to-nose calibration," in *55th ARFTG Conf. Dig.*, Jun. 2000, vol. 116, pp. 1–6.

[13] D. F. Williams, T. S. Clement, P. D. Hale, and A. Dienstfrey, "Terminology for high-speed sampling-oscilloscope calibration," in *68th ARFTG Microw. Meas. Conf. Dig.*, Boulder, CO, Nov. 30–Dec. 1 2006, pp. 9–14.

[14] P. D. Hale and C. M. Wang, "Calculation of pulse parameters and propagation of uncertainty," *IEEE Trans. Instrum. Meas.*, vol. 58, no. 3, pp. 639–648, Mar. 2009.

[15] D. F. Williams, A. Lewandowski, T. S. Clement, C. M. Wang, P. D. Hale, J. M. Morgan, D. A. Keenan, and A. Dienstfrey, "Covariance-based uncertainty analysis of the NIST electrooptic sampling system," *IEEE Trans. Microw. Theory Tech.*, vol. 54, no. 1, pp. 481–491, Jan. 2006.

[16] M. Cox, M. Dainton, P. Harris, and N. Ridler, "The evaluation of uncertainties in the analysis of calibration data," in *IEEE Instrum. Meas. Conf.*, May 24–26, 1999, pp. 1093–1098.

[17] T. Daboczi, "Nonparametric identification assuming two noise sources: A deconvolution approach," *IEEE Trans. Instrum. Meas.*, vol. 47, no. 4, pp. 828–832, Aug. 1998.

[18] P. D. Hale, D. F. Williams, A. Dienstfrey, C. M. Wang, A. Lewandowski, T. S. Clement, and D. A. Keenan, "Complete waveform characterization at NIST," in *Conf. Precision Electromagn. Meas.*, Jun. 8–13, 2008, pp. 680–681.

[19] P. D. Hale, C. M. Wang, D. F. Williams, K. A. Remley, and J. Wepman, "Compensation of random and systematic timing errors in sampling oscilloscopes," *IEEE Trans. Instrum. Meas.*, vol. 55, no. 6, pp. 2146–2154, Dec. 2006.

[20] N. G. Paulter, "Low-jitter trigger system for pulse calibration and intercomparison of high-speed samplers," *IEEE Trans. Instrum. Meas.*, vol. 47, no. 3, pp. 606–608, Jun. 2006.

[21] *Timebase Correction Software*. [Online]. Available: http://www.boulder.nist.gov/div815/HSM_Project/HSMP.htm

[22] P. T. Boggs, R. H. Byrd, and R. B. Schnabel, "A stable and efficient algorithm for nonlinear orthogonal distance regression," *SIAM J. Sci. Stat. Comput.*, vol. 8, no. 6, pp. 1052–1078, Nov. 1987.

[23] T. S. Clement, P. D. Hale, D. F. Williams, C. M. Wang, A. Dienstfrey, and D. A. Keenan, "Calibration of sampling oscilloscopes with high-speed photodiodes," *IEEE Trans. Microw. Theory Tech.*, vol. 54, no. 8, pp. 3173–3181, Aug. 2006.

[24] Y. Rolain, J. Schoukens, and G. Vandersteen, "Signal reconstruction for non-equidistant finite length sample sets: A 'KIS' approach," *IEEE Trans. Instrum. Meas.*, vol. 47, no. 5, pp. 1046–1052, Oct. 1998.

[25] M. Unser, "Sampling—50 years after Shannon," *Proc. IEEE*, vol. 88, no. 4, pp. 569–587, Apr. 2000.

[26] D. F. Williams, P. D. Hale, T. S. Clement, and J. M. Morgan, "Calibrating electro-optic sampling systems," in *IMS Conf. Dig.*, May 2001, vol. 1473, pp. 1527–1530.

[27] T. S. Clement, D. F. Williams, P. D. Hale, and J. M. Morgan, "Calibrated photoreceiver response to 110 GHz," in *Conf. Dig. 15th Annu. Meeting IEEE Lasers Electro-Optics Soc.*, Glasgow, U.K., Nov. 10–14, 2002, pp. 877–878.

[28] A. Dienstfrey, P. D. Hale, D. A. Keenan, T. S. Clement, and D. F. Williams, "Minimum-phase calibration of sampling oscilloscopes," *IEEE Trans. Microw. Theory Tech.*, vol. 54, no. 8, pp. 3197–3208, Aug. 2006.

[29] D. F. Williams, C. M. Wang, and U. Arz, "An optimal vector-network-analyzer calibration algorithm," *IEEE Trans. Microw. Theory Tech.*, vol. 51, no. 12, pp. 2391–2401, Dec. 2003.

[30] N. G. Paulter and R. B. Stafford, "Reducing the effects of record truncation discontinuities in waveform reconstruction," *IEEE Trans. Instrum. Meas.*, vol. 42, no. 3, pp. 695–700, Jun. 1993.

[31] A. N. Tikhonov and V. Y. Arsenin, *Solutions of Ill-Posed Problems*. Washington, DC: V.H. Winston and Sons, 1977.

[32] P. C. Hansen, *Rank-Deficient and Discrete Ill-Posed Problems*. Philadelphia, PA: SIAM, 1997.

[33] H. W. Engle, M. Hanke, and A. Neubauer, *Regularization of Inverse Problems*. Norwell, MA: Kluwer, 2000.

[34] W. L. Gans, "Calibration and error analysis of a picosecond pulse waveform measurement system at NBS," *Proc. IEEE*, vol. 74, no. 1, pp. 86–90, Jan. 1986.

[35] BIPM, IEC, IFCC, ISO, IUPAC, IUPAP, and OIML, *Guide to the Expression of Uncertainty in Measurement*, pp. 1–101, 1993, International Organization for Standardization.

[36] J. Mandel, *The Statistical Analysis of Experimental Data*. New York: Dover, 1984.

[37] F. A. Graybill, *Theory and Application of the Linear Model*. North Scituate, MA: Duxbury, 1976.

[38] C. M. Wang, P. D. Hale, and D. F. Williams, "Uncertainty of timebase corrections," *IEEE Trans. Instrum. Meas.*, vol. 58, no. 10, pp. 3468–3472, Oct. 2009.

[39] J. A. Hartigan, *Clustering Algorithms*. New York: Wiley, 1975.

[40] L. Kaufman and P. Rousseeuw, *Finding Groups in Data: An Introduction to Cluster Analysis*. New York: Wiley, 2005.

[41] P. Rousseeuw and A. Leroy, *Robust Regression and Outlier Detection*. New York: Wiley, 2004.

[42] A. Papoulis, *The Fourier Integral and Its Applications*. New York: McGraw-Hill, 1987.

[43] A. M. Nicolson, "Forming the fast Fourier transform of a step response in time-domain metrology," *Electron. Lett.*, vol. 9, no. 14, pp. 317–318, Jul. 12, 1973.
[44] J. Waldmeyer, "Fast Fourier transform for step-like functions: The synthesis of three apparently different methods," *IEEE Trans. Instrum. Meas.*, vol. IM-29, no. 1, pp. 36–39, Mar. 1980.

Paul D. Hale (M'01–SM'01) received the Ph.D. degree in applied physics from the Colorado School of Mines, Golden, in 1989.

Since 1989, he has been with the Optoelectronics Division, National Institute of Standards and Technology (NIST), Boulder, CO, where he conducts research on broadband optoelectronic device and signal metrology. He has been the Leader of the High-Speed Measurements Project in the Sources and Detectors Group since 1996. He is the author of over 60 published technical papers.

Dr. Hale was an Associate Editor of the Optoelectronics/Integrated Optics for the IEEE JOURNAL OF LIGHTWAVE TECHNOLOGY from June 2001 to March 2007. He is the recipient of the Department of Commerce Bronze, Silver, and Gold Awards, two Automatic RF Techniques Group Best Paper Awards, and the NIST Electrical Engineering Laboratory's Outstanding Paper Award.

Andrew Dienstfrey received the B.A. degree in mathematics from Harvard College, Cambridge, MA, in 1990 and the Ph.D. degree in mathematics from the Courant Institute of Mathematical Sciences, New York, in 1998.

From 1998 to 2000, he was a Postdoctoral Scientist with the Courant Institute, investigating methods for remote sensing of dielectric properties of superconducting thin films. He joined the Mathematical and Computational Sciences Division, National Institute of Standards and Technology, Boulder, CO, in 2000. His research interests include theoretical and computational aspects of periodic scattering problems in acoustics and electromagnetics.

Jack C. M. Wang received the Ph.D. degree in statistics from Colorado State University, Fort Collins, in 1978.

He joined the Statistical Engineering Division, National Institute of Standards and Technology, Boulder, CO, in 1988. He is the author of over 80 published journal articles. His research interests include statistical metrology and the application of statistical methods to physical sciences.

Dr. Wang is a Fellow of the American Statistical Association (ASA). He is the recipient of the Department of Commerce Bronze Medal and several awards from ASA.

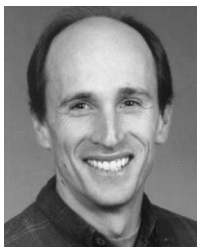

Dylan F. Williams (M'80–SM'90–F'02) received the Ph.D. degree in electrical engineering from the University of California, Berkeley, in 1986.

He joined the Electromagnetic Fields Division, National Institute of Standards and Technology, Boulder, CO, in 1989, where he develops metrology for the characterization of monolithic microwave integrated circuits and electronic interconnects. He is the author of over 80 published technical papers.

Dr. Williams is currently the Editor of the IEEE TRANSACTIONS ON MICROWAVE THEORY AND TECHNIQUES. He is the recipient of the Department of Commerce Bronze and Silver Medals, two Electrical Engineering Laboratory's Outstanding Paper Awards, two Automatic RF Techniques Group (ARFTG) Best Paper Awards, the ARFTG Automated Measurements Technology Award, and the IEEE Morris E. Leeds Award.

Arkadiusz Lewandowski (S'02) was born in Poland in 1975. He received the M.Sc. degree in electrical engineering in 2001 from Warsaw University of Technology, Warsaw, Poland, where he is currently working toward the Ph.D. degree in microwave measurements.

In 2002, he joined the Institute of Electronics Systems, Warsaw University of Technology. From 1999 to 2000, he was with the Department of High Frequency Techniques, University of Kassel, Kassel, Germany, working on the design of microwave oscillators. From 2002 to 2004, he was involved in the development of digital synthesizers of radar signals with the Telecommunications Research Institute, Warsaw. He is currently a Guest Researcher with the National Institute of Standards and Technology (NIST), Boulder, CO, where he is engaged in the development of VNA calibration methods applicable for time-domain measurements. His current research interests include VNA calibration techniques and on-wafer microwave measurements.

Mr. Lewandowski was the recipient of Best Paper Award at the International Microwave Conference MIKON 2008, Poland, the 2005 MTT-S Graduate Fellowship Award, the Second Prize of AP/AES/MTT Joint Chapter of the Poland Section of IEEE for the best M.Sc. thesis, and the Second Prize of EuMA for the Best Student Paper at the International Microwave Conference MIKON 2002, Poland.

Darryl A. Keenan received the B.S. degree in physics from the University of Colorado, Fort Collins, in 1996.

In 1989, he joined the National Institute of Standards and Technology and has since been a member of the Sources and Detectors Group of the Optoelectronics Division. He has run optical laser metrology laboratories, including low-power CW from the visible to near infrared, high-power CW at far infrared, Q-switched Nd:YAG at near infrared, and excimer at ultraviolet to deep ultraviolet. He has worked with colleagues to develop optical fiber connector characterization and to develop a system for measuring detector nonlinearity at 193 nm. His current areas of research are in time- and frequency-domain characterization of oscilloscopes and photodiodes.

Tracy S. Clement (S'89–M'92–SM'05) received the Ph.D. degree in electrical engineering from Rice University, Houston, TX, in 1993. Her Ph.D. research involved developing and studying a variety of ultrashort pulse and very short wavelength lasers.

Since 1998, she has been with the Optoelectronics Division of the National Institute of Standards and Technology (NIST), Boulder, CO. Her current research interests include the development of measurement systems for high-speed electro-optic components as well as ultrashort pulse laser measurements. Prior to joining the Optoelectronics Division, she was an Associate Fellow of JILA and the Quantum Physics Division of NIST and was an Assistant Professor Adjoint in the Department of Physics, University of Colorado, Boulder. From 1993 to 1995, she was a Director's Postdoctoral Fellow at Los Alamos National Laboratory, Los Alamos, NM.